

## Optical Properties of Shallow Convective Clouds Diagnosed from a Bulk-Microphysics Large-Eddy Simulation

JOANNA SLAWINSKA

*Institute of Geophysics, University of Warsaw, Warsaw, Poland*

WOJCIECH W. GRABOWSKI

*National Center for Atmospheric Research,\* Boulder, Colorado*

HANNA PAWLOWSKA

*Institute of Geophysics, University of Warsaw, Warsaw, Poland*

ANDRZEJ A. WYSZOGRODZKI

*National Center for Atmospheric Research,\* Boulder, Colorado*

(Manuscript received 14 December 2006, in final form 20 July 2007)

### 1. Introduction

Large-eddy simulation (LES) models provide an indispensable tool to study processes within cloud-topped subtropical and trade wind boundary layers (e.g., Siebesma et al. 2003; Stevens et al. 2005, and references therein). Typically, LES models use bulk representation of cloud microphysics. Bulk approach assumes that warm (ice free) clouds are exactly at water saturation and that a cloud cannot exist in undersaturated conditions. It is well established from cloud observations (e.g., Stommel 1947; Warner 1955; Blyth 1993; Wang and Albrecht 1994) and cloud modeling (e.g., Brenguier and Grabowski 1993; Carpenter et al. 1998; Siebesma et al. 2003; Chosson et al. 2007) that shallow cumulus and stratocumulus clouds are strongly diluted by entrainment and that such dilution affects not only bulk thermodynamic properties [e.g., the liquid water content (LWC)] but also cloud microphysics (i.e., the spectrum of cloud droplets). For nonprecipi-

tating clouds, conservation of total water (vapor plus liquid) and moist static energy determines bulk thermodynamic properties of cloud volumes diluted by entrainment of environmental air. Predicting changes of the cloud droplet spectra resulting from entrainment, on the other hand, requires additional constraints because situations where cloud water after homogenization is distributed over either the same number of smaller droplets (i.e., the homogeneous mixing scenario) or smaller number of droplets with the initial size (i.e., the extremely inhomogeneous mixing scenario; Baker and Latham 1979; Baker et al. 1980) are equally possible (see discussion in Andrejczuk et al. 2006).

The impact of entrainment and mixing on cloud droplet spectra has been shown to significantly affect mean radiative properties of a field of stratocumulus and cumulus clouds. Chosson et al. (2004) were first to show this for the case of stratocumulus. They examined the impact of microphysical transformation following entrainment and mixing by considering separately the homogeneous and extremely inhomogeneous mixing scenarios and showed that the mean cloud optical thickness derived by applying the homogeneous scheme was about 35% larger than for the extremely inhomogeneous mixing (see Chosson et al. 2007 for further discussion). This result prompted an investigation reported in Grabowski (2006, hereafter G06), where a similar issue was investigated in the context of

---

*Corresponding author address:* Wojciech W. Grabowski, NCAR/MMM, P.O. Box 3000, Boulder, CO 80307-3000.  
E-mail: grabow@ncar.ucar.edu

---

\* The National Center for Atmospheric Research is sponsored by the National Science Foundation.

convective–radiative quasi equilibrium mimicking the mean conditions on the earth and with the emphasis on the indirect aerosol effects. Two limits of the concentration of cloud droplets  $n_o$  were considered, either  $n_o = 100 \text{ cm}^{-3}$ , referred to as PRISTINE, or  $n_o = 1000 \text{ cm}^{-3}$ , referred to as POLLUTED. The 2D model used in G06's study applied bulk microphysics and, similarly to Chosson et al. (2004, 2007), required additional assumptions concerning sizes of cloud droplets when coupled to the radiative transfer model. The relevant parameter is the effective radius, the ratio between the third and the second moment of the cloud droplets size distribution (e.g., Stephens 1978). Effective radius has been shown to be slightly larger than the mean volume radius (e.g., Martin et al. 1994; Pawlowska and Brenguier 2000). In G06's study, the formulation of the effective radius in the diluted cloudy volumes turned out to be of critical importance, with the mean top-of-the-atmosphere (TOA) albedo (and thus the amount of solar energy reaching the surface) being the same in the PRISTINE case assuming the homogeneous mixing scenario and in the POLLUTED case with the extremely inhomogeneous mixing.

As on the earth, the model cloudiness in G06 was dominated by shallow convection. However, since the model setup was designed with the deep convection in mind, the horizontal resolution was not adequate for shallow clouds. Moreover, the model applied 2D geometry, which also limits the generality of conclusions. It follows that it would be desirable to perform a similar investigation using a 3D model with a spatial resolution appropriate for shallow clouds, that is, using a LES model. This paper reports results of such an investigation. The next section briefly discusses the model and modeling setup. Section 3 provides details of the formulation of effective radius applying various assumptions concerning the local concentration of cloud droplets. Vertical profiles of the diagnosed effective radius are presented in section 4, together with results of radiation transfer model applied offline to the cloud data. Brief discussion of model results in section 5, including a comparison with observations reported in McFarlane and Grabowski (2007), concludes the paper.

## 2. The model and modeling setup

The model used in this study is the 3D anelastic semi-Lagrangian–Eulerian model EULAG documented in Smolarkiewicz and Margolin (1997, model dynamics), Grabowski and Smolarkiewicz (1996, model thermodynamics), and Margolin et al. (1999, subgrid-scale turbulent mixing). In this study, EULAG is set up to simulate steady-state trade wind shallow nonprecipitating

convection observed during the Barbados Oceanographic and Meteorological Experiment (BOMEX; Holland and Rasmusson 1973) and recently used in the model intercomparison study described in Siebesma et al. (2003). In the BOMEX case, the 1.5-km-deep trade wind convection layer overlays 0.5-km-deep mixed layer near the ocean surface and is covered by 500-m-deep trade wind inversion layer. The cloud cover is about 10% and quasi-steady conditions are maintained by the prescribed large-scale subsidence, large-scale moisture advection, surface heat fluxes, and radiative cooling. The model setup is exactly as described in Siebesma et al. (2003). The horizontal/vertical grid length is 100 m/40 m and model time step is 3 s. As in Siebesma et al. (2003), the model is run for 6 h, and results from the last 4 h are used in the analysis.

In general, EULAG results fall within the spread of all models presented in Siebesma et al. (2003). It follows that EULAG simulation faithfully represents gross features of the trade wind convection observed in BOMEX, including mean thermodynamic and wind profiles, mean characteristics of the cloud field (e.g., the cloud cover and liquid water path), and mean profiles of the temperature and moisture fluxes between the surface and trade wind inversion. A single simulation (archived every 10 min of the model time) is used in the analysis presented in this paper. This is because, unlike in G06, effective radius and optical thickness are only diagnosed using various assumptions concerning the mixing between clouds and their environment. Furthermore, we apply a solar radiation transfer model (the same as in G06) to document the impact of the diagnosed effective radius on the mean cloud albedo and on the net solar flux at the surface.

## 3. Derivation of the effective radius from bulk model output

As suggested by Martin et al. [1994, Eq. (10) therein], the effective radius  $r_e$  is assumed proportional to the mean volume radius  $r_v$ :

$$r_v^3 = k r_e^3, \quad (1)$$

where  $k = 0.80$  for the PRISTINE and  $k = 0.67$  for the POLLUTED. The mean volume radius  $r_v$ , on the other hand, is locally defined as

$$r_v = \left( \frac{3\text{LWC}}{4\pi\rho_w n} \right)^{1/3}, \quad (2)$$

where  $\rho_w = 10^3 \text{ kg m}^{-3}$  is the water density, and LWC and  $n$  are the local values of the liquid water content and concentration of cloud droplets, respectively. Note

that EULAG predicts LWC, but not  $n$ , and additional assumptions are needed to predict local values of  $r_v$  and thus  $r_e$ . Four different assumptions concerning variability of  $n$  are reviewed below and are later used in the analysis of the model output.

*a. Uniform cloud droplet concentration,  $r_v^{(u)}$ , and  $r_e^{(u)}$*

In this case, it is assumed that the concentration of cloud droplets does not change within a cloud and it is taken in (2) as  $n = n_o$  (i.e., either  $100 \text{ cm}^{-3}$  for the PRISTINE or  $1000 \text{ cm}^{-3}$  for POLLUTED). This case was referred to as the homogeneous mixing scenario in G06. It was recognized, however, that this is an approximation because the homogeneous mixing involves also a change of droplet concentration, with the concentration in a diluted parcel smaller by a factor of  $\chi$ , the proportion of the cloudy air in the mixture (see discussion below and in the appendix in G06).

*b. Homogeneous mixing scenario,  $r_v^{(h)}$ , and  $r_e^{(h)}$*

In this case, it is assumed that the concentration of cloud droplets changes within a cloud only because of the dilution due to entrainment. It follows that  $n$  is taken as  $n = \chi n_o$  in (2), where, again,  $n_o = 100 \text{ cm}^{-3}$  for the PRISTINE and  $1000 \text{ cm}^{-3}$  for POLLUTED. The proportion of the cloudy air in the mixture  $\chi$  is approximated, assuming that the total water at a given location is a linear combination of the total water  $Q$  inside the adiabatic parcel raising from the cloud base and an unsaturated environmental air at this level:

$$Q = \chi Q^a + (1 - \chi) Q^e, \quad (3)$$

where  $Q = q_v + q_c$  ( $q_v$  and  $q_c$  are the water vapor and cloud water mixing ratios), and superscripts  $a$  and  $e$  refer to the adiabatic and environmental values, respectively. Note that (3) represents an extreme simplification of the entrainment problem in cumulus clouds (cf. Blyth 1993). Since there is no precipitation,  $Q^a$  is equal to the total water at the cloud base. The environmental total water  $Q^e = q_v^e$  can be approximated as the mean over cloud-free grid boxes at this level. It follows from (3) that

$$\chi = \max \left[ 0, \min \left( 1, \frac{Q - Q^e}{Q^a - Q^e} \right) \right], \quad (4)$$

where additional limiting ensures only physically realizable values of  $\chi$ . Adiabatic parcel analysis is performed using cloud-base conditions obtained by conditional sampling (i.e., considering only points with  $q_c > 10^{-5} \text{ kg kg}^{-1}$ ) at a height of 600 m, which is within

the range of simulated cloud-base heights for various clouds during the 4-h analysis period. In summary, local values of  $\chi$  are deduced from (4) and later used in (2) with  $n = \chi n_o$  to derive  $r_v^{(h)}$ .

*c. Intermediate mixing scenario,  $r_v^{(in)}$ , and  $r_e^{(in)}$*

In this case, it is assumed that the concentration of cloud droplets changes within a cloud because of the dilution due to entrainment and that the change in droplet concentration is the same as the change of the mean volume radius cubed. Such a mixing scenario was suggested by direct numerical simulations of interfacial mixing at low turbulence levels discussed in Andrejczuk et al. (2006). In such a mixing scenario, the mean volume radius is prescribed as (see appendix in G06)

$$r_v = \beta^{1/6} r_v^a, \quad \beta = \min \left( 1, \frac{\text{LWC}}{\chi \text{LWC}^a} \right), \quad (5)$$

where  $\text{LWC}^a$  and  $r_v^a$  are the adiabatic liquid water content and the adiabatic mean volume radius [i.e.,  $\text{LWC}^a = 4/3 \pi (r_v^a)^3 n_o \rho_w$ ]. The limiting in (5) ensures only physically realizable values of  $\beta$ .

*d. Extremely inhomogeneous mixing scenario,  $r_v^{(ei)}$ , and  $r_e^{(ei)}$*

In this case, it is assumed that entrainment changes only the concentration of cloud droplets without affecting the mean volume radius. In this case,

$$r_v = r_v^a. \quad (6)$$

The above four formulations of  $r_v$  result in various spatial distributions of  $r_e$ , separately for the PRISTINE and POLLUTED cases (i.e., choosing  $n_o$  as either 100 or  $1000 \text{ cm}^{-3}$ ). Selected statistics of these distributions are compared in the next section. Moreover, in each cloudy column, the cloud optical thickness can be derived as  $\tau = 1.5/\rho_w \int \text{LWC}/r_e dz$ , with  $r_e$  defined in various ways as discussed above. Finally, a radiation transfer model can be applied to cloudy columns to assess the impact of various mixing scenarios on solar radiation.

## 4. Results

Figure 1 presents the contoured frequency by altitude diagrams (CFADs) of  $r_e$  derived according to the scenarios 1 to 4 and for PRISTINE and POLLUTED conditions. As expected, mean  $r_e$  increases with height in all scenarios. A noisy pattern near cloud tops in mixing scenarios 1–3 most likely reflects poor sampling of the deepest clouds. For a given formulation, POLLUTED cases show significantly smaller  $r_e$  when

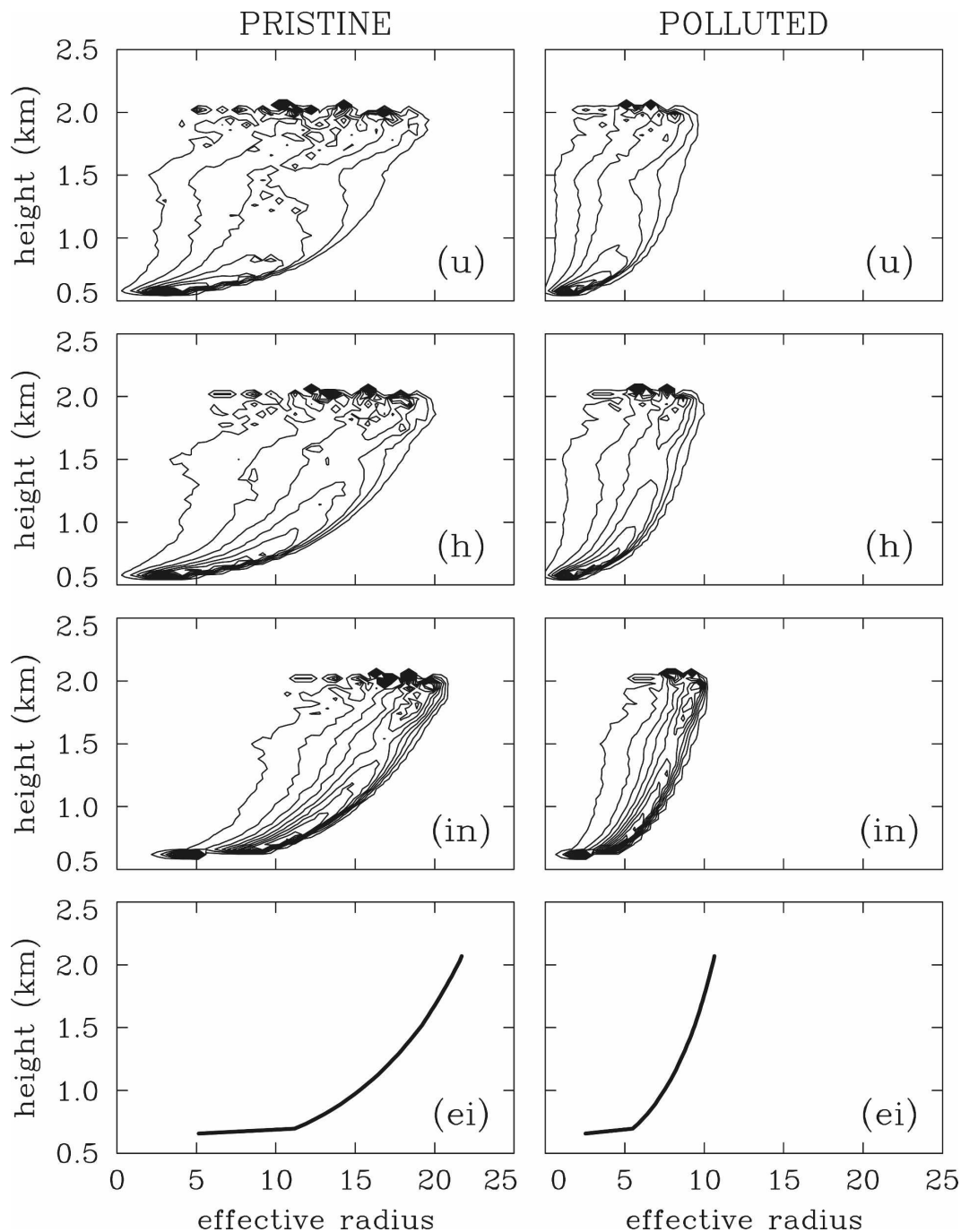


FIG. 1. CFADs of the diagnosed effective radius assuming (left) PRISTINE and (right) POLLUTED conditions. Panels represent (from top to bottom) uniform droplet concentration (u), homogeneous (h), intermediate (in), and extremely inhomogeneous (ei) mixing scenarios. Bin size is  $0.5 \mu\text{m}$ . Frequency is contoured starting at 1% with contour interval of 2% and 4% for PRISTINE and POLLUTED, respectively. Note that for (ei) all contours collapse into a single profile.

compared to the PRISTINE. Since the uniform scenario does not consider dilution of droplet concentration due to entrainment, it results in the smallest droplet sizes compared to other scenarios. The mean  $r_e$  at a

given height gradually increases when one moves across mixing scenarios from uniform droplet concentration to the extremely inhomogeneous mixing. The effective radius in the extremely inhomogeneous mixing (i.e., the

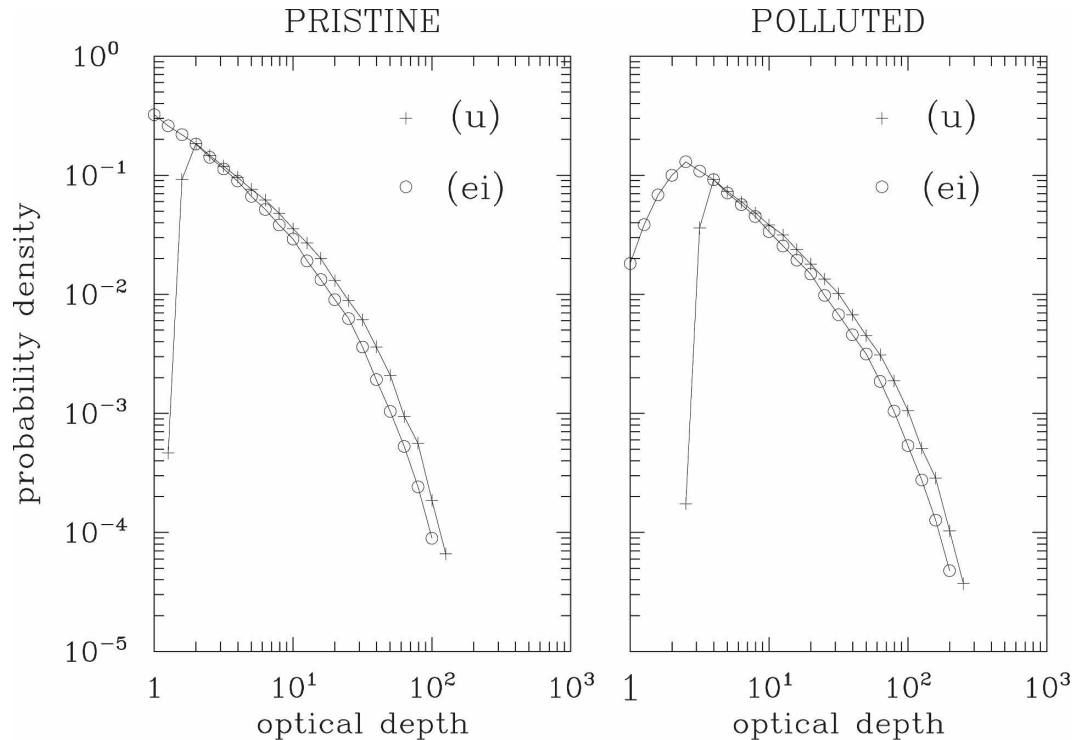


FIG. 2. PDFs of the optical thickness derived from model columns with LWP larger than  $5 \times 10^{-3} \text{ kg m}^{-2}$  and for (left) PRISTINE and (right) POLLUTED conditions. Only data for uniform droplet concentration (u) and extremely inhomogeneous mixing (ei) are shown.

adiabatic  $r_e$ ) is larger than the maximum  $r_e$  predicted by any other mixing scenario at the same height. This attests to the significant dilution of shallow convective clouds simulated in this study, which is best illustrated by a CFAD of the adiabatic fraction  $\text{LWC}/\text{LWC}^a$  (not shown; cf. Fig. 7 in Siebesma et al. 2003). At any level, the uniform droplet concentration results in a histogram with the largest width. The difference between uniform droplet concentration and homogeneous mixing is significant, an effect neglected in G06. Of a particular relevance is the fact that the adiabatic  $r_e$  for the extremely inhomogeneous mixing in POLLUTED is close to the mean  $r_e$  for the uniform droplet concentration in PRISTINE; that is,  $r_e$  in both cases is in the range between 5 and  $10 \mu\text{m}$  across most of the cloud depth.

Figure 2 shows probability density functions (PDFs) of the optical thickness  $\tau$  for PRISTINE and POLLUTED and for uniform droplet concentration and extremely inhomogeneous mixing (i.e., the two scenarios that provide limiting sizes of  $r_e$  for either PRISTINE or POLLUTED case). Only model columns with liquid water path (LWP) larger than  $5 \times 10^{-3} \text{ kg m}^{-2}$  are included in the analysis. Because of the limited vertical extent of BOMEX clouds, values of the optical

thickness larger than 100 are rare, unlike in the case of convective–radiative equilibrium of G06, which featured deep as well as shallow clouds. The PDFs are similar to those in G06 (Fig. 5 therein), with maximum values for  $\tau < 10$  and long tails extending to values  $\tau \sim 100$ . As in Fig. 5 of G06, changing mixing scenario from the uniform droplet concentration to the extremely inhomogeneous mixing leads to a decrease of PDF for small  $\tau$ s and an increase for  $\tau > 10$ . However, changes in the PDFs between PRISTINE and POLLUTED cases are smaller than in G06, consistent with only the first indirect effect considered here (i.e., changes of  $r_e$  alone), whereas both the first and the second indirect effects were considered in G06 (i.e., changes in both  $r_e$  and LWP).

To document the impact of various mixing scenarios on mean optical properties of the cloud field, the two-stream radiation transfer model was applied column by column (i.e., in the independent column approximation mode) to the cloud model data combined with the diagnosed effective radius of cloud droplets (i.e., similarly to Chosson et al. 2004, 2007). The radiation transfer model, the same as in G06, comes from the National Center for Atmospheric Research (NCAR) Community Climate System Model (Kiehl et al. 1994). The

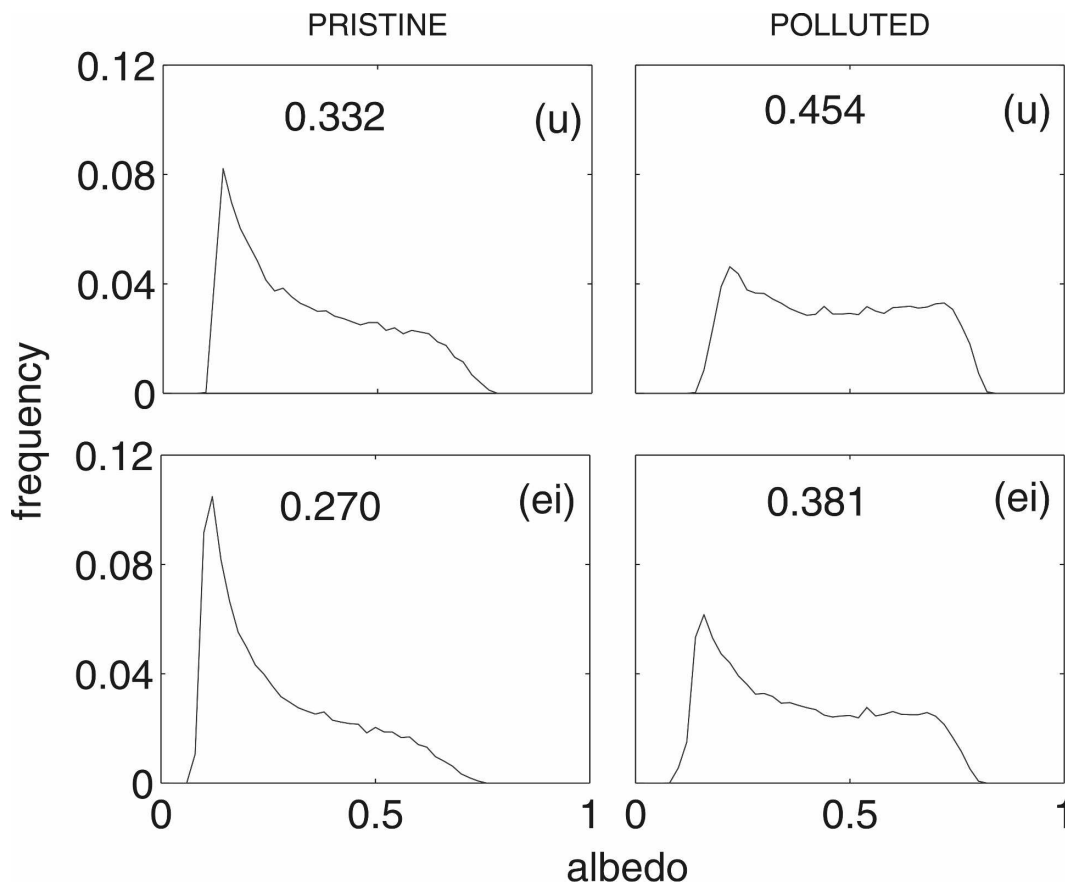


FIG. 3. Histograms of cloud TOA albedo for model columns with LWP larger than  $5 \times 10^{-3} \text{ kg m}^{-2}$  for (left) PRISTINE and (right) POLLUTED conditions. (top) Uniform droplet concentration and (bottom) extremely inhomogeneous mixing. The width of the albedo bin is 0.02. Mean albedo is shown in each panel.

solar constant is taken as  $436 \text{ W m}^{-2}$  (i.e., the nominal solar constant at an equinox divided by  $\pi$  to represent insolation averaged over the diurnal cycle) and a zero zenith angle is assumed. Figure 3 shows histograms of the TOA cloud albedo for PRISTINE and POLLUTED and for the uniform droplet concentration and the extremely inhomogeneous mixing (i.e., the two scenarios that provide limiting sizes of  $r_e$  for either PRISTINE or POLLUTED case). As in Fig. 2, only model columns with LWP larger than  $5 \times 10^{-3} \text{ kg m}^{-2}$  are included in the analysis.<sup>1</sup> As Fig. 3 shows, the range

of TOA albedos for cloudy columns is between 0.1 and 0.7, with consistent changes for different local mixing scenarios. For instance, the change from uniform droplet concentration to extremely inhomogeneous mixing (i.e., with larger cloud droplets diagnosed in diluted cloud volumes) results in reduced frequencies for high albedos and corresponding increase of the peak for albedos around 0.1. This is true for both PRISTINE and POLLUTED cases.

Model results for various mixing scenarios are summarized in Table 1. The table shows averaged values of the mean optical thickness  $\tau$ , the mean “effective”  $r_e$ , the mean cloud TOA albedo  $A_{\text{cloudy}}$ , and the mean net solar flux at the surface  $\text{SF}_{\text{cloudy}}$ , all calculated including only model columns with the LWP larger than  $5 \times 10^{-3} \text{ kg m}^{-2}$ , as in Figs. 2 and 3. The effective  $r_e$  is calculated in each column using the LWP and the optical thickness  $\tau$  as  $\bar{r}_e = 1.5 \text{ LWP}/(\rho_w \tau)$  [cf. Eq. (3) in G06]; its averaged value (for columns with the LWP larger than  $5 \times 10^{-3} \text{ kg m}^{-2}$ ) is shown in the table. The conditionally aver-

<sup>1</sup> If all model columns are considered, the histogram is dominated by clear-sky values because the cloud cover in BOMEX is relatively low (around 10%, cf. Fig. 2a in Siebesma et al. 2003). The mean TOA albedo of the scene can be calculated as  $(1 - \delta)A_{\text{clear}} + \delta A_{\text{cloudy}}$ , where  $\delta$  is the cloud cover and  $A_{\text{clear}}$  ( $\approx 0.05$ , mostly due to the assumed albedo of the ocean surface) and  $A_{\text{cloudy}}$  are the mean albedos of clear-sky and cloudy columns, respectively.

TABLE 1. Mean values of the optical thickness  $\tau$ ,  $\bar{r}_e$ , TOA albedo  $A_{\text{cloudy}}$ , and net solar flux at the surface  $SF_{\text{cloudy}}$  for various mixing scenarios. Only model columns with LWP larger than  $5 \times 10^{-3} \text{ kg m}^{-2}$  are included in the analysis. See text for details.

| Mixing scenario                            | PRISTINE |       |       |       | POLLUTED |       |       |       |
|--|----------|-------|-------|-------|----------|-------|-------|-------|
|  | (u)      | (h)   | (in)  | (ei)  | (u)      | (h)   | (in)  | (ei)  |
| $\tau$ (1)                                 | 11.5     | 10.4  | 9.0   | 7.7   | 23.5     | 21.2  | 18.3  | 15.8  |
| $\bar{r}_e$ ( $\mu\text{m}$ )              | 8.1      | 9.1   | 11.1  | 13.6  | 4.0      | 4.4   | 5.4   | 6.7   |
| $A_{\text{cloudy}}$ (1)                    | 0.332    | 0.320 | 0.292 | 0.270 | 0.454    | 0.441 | 0.409 | 0.381 |
| $SF_{\text{cloudy}}$ ( $\text{W m}^{-2}$ ) | 229      | 234   | 245   | 255   | 177      | 182   | 196   | 208   |

aged liquid water path is  $8 \times 10^{-2} \text{ kg m}^{-2}$  (i.e., 3 to 4 times smaller than in the deep convection case of G06, Table 3 therein). In general, changes of the mean optical thickness and effective radius between PRISTINE and POLLUTED with various mixing scenarios in this study are similar to the changes reported in G06 (Table 3 therein). For instance, the mean optical thickness for PRISTINE with uniform droplet concentration is 11.5 and it is 15.8 for POLLUTED with extremely inhomogeneous mixing; that is, it changes by a factor of 1.4 between the two cases. Corresponding values are 32.1 and 57.4 in G06, which implies a factor of 1.8. For the mean effective  $r_e$ , corresponding values are 8.1 and 6.7  $\mu\text{m}$  in this study and 8.3 and 7.4  $\mu\text{m}$  in G06. Unlike in G06, the mean albedo for PRISTINE with uniform droplet concentration is smaller than for POLLUTED with extremely inhomogeneous mixing (0.33 versus 0.38), and the difference is comparable to the range observed for either PRISTINE or POLLUTED (from 0.27 to 0.33 or 0.38 to 0.45). For the  $SF_{\text{cloudy}}$ , the differences between different mixing scenarios seem larger than in G06 (i.e., the change here is about 30  $\text{W m}^{-2}$  from uniform droplet concentration to extremely inhomogeneous mixing compared to about 20  $\text{W m}^{-2}$  in G06). One needs to keep in mind, however, that a different incoming solar flux was applied here than in G06 (436 versus 342  $\text{W m}^{-2}$ ), and that results in Table 1 only include cloudy columns. Nevertheless, the overall impact of mixing scenarios in 3D LES simulations discussed here is consistent with results discussed in G06. In particular, POLLUTED clouds assuming extremely inhomogeneous mixing scenario have optical properties not far from PRISTINE clouds with uniform droplet concentration.

## 5. Discussion and conclusions

Results presented in this paper strongly support predictions of the low-resolution 2D study by G06 that the formulation of the effective radius in diluted volumes of shallow convective clouds plays an essential role in

mean optical properties of a cloud field and thus in the mean TOA albedo of an ensemble of clouds. Such a conclusion is also consistent with results discussed in Chosson et al. (2004, 2007) for the case of stratocumulus. In the current investigation, similarly to G06, POLLUTED clouds assuming extremely inhomogeneous mixing scenario have optical properties similar to PRISTINE clouds with uniform droplet concentration.

Results presented here can be compared to the observational study of McFarlane and Grabowski (2007) where a CFAD of the effective radius and a PDF of the cloud optical thickness were derived from ground-based remote sensing of shallow tropical clouds over the Atmospheric Radiation Measurement Program (ARM) tropical western Pacific Nauru site using the technique described in McFarlane et al. (2002). As documented in McFarlane and Grabowski (2007, their Fig. 2), the CFAD of retrieved  $r_e$  has significant width, which increases with height, and tends to have a bimodal shape with wide peaks that limit the variability of  $r_e$ . The peak at small  $r_e$  represents cloud droplets with sizes not much different than those near the cloud base, suggesting a new activation of cloud droplets due to entrainment. The peak at large  $r_e$ , while representing much larger droplets, is still significantly smaller than the adiabatic size. CFADs derived from model results presented here have different shapes. The extremely inhomogeneous mixing scenario between the adiabatic cloud and its unsaturated environment predicts adiabatic  $r_e$  at a given height and is thus inconsistent with the observations. All three other mixing scenarios predict distributions of  $r_e$  with a significant width (as in observations) but with only one peak, somewhere between the adiabatic size and the cloud-base size. Despite these differences, the PDFs of the optical thickness are similar to the one derived from the observations (Fig. 4 in McFarlane and Grabowski 2007), with the maxima for low  $\tau$ s around 0.1 and PDFs decreasing to about  $10^{-4}$  for  $\tau = 100$ .

The above comparison suggests that the spatial variability of  $r_e$  in real clouds is more complicated than the

variability predicted by simple models of microphysical transformations considered in this study. Variable in time and space transformations associated with the cloud–environment mixing (resulting in a superposition of CFADs shown in Fig. 1), combined with additional nucleation of cloud droplets above the cloud base either due to increasing updraft strength or due to entrainment (see discussion in McFarlane and Grabowski 2007), can all contribute to the observed variability. This subject will be further investigated using a newly developed two-moment warm rain bulk microphysics scheme (i.e., predicting both the number of cloud droplets and their mixing ratio), capable of predicting drizzle/rain formation as well as changes of the supersaturation field within shallow ice-free clouds (and thus the in-cloud nucleation), and including various scenarios of microphysical transformations due to turbulent entrainment and mixing (Morrison and Grabowski 2007, 2008). Such simulations will allow studying both the first and the second indirect effect using the BOMEX case considered here, as well as the precipitating shallow convection case based on observations during the Rain in Cumulus over the Ocean (RICO) experiment (see <http://www.knmi.nl/samenw/rico/>). Moreover, 3D radiative transfer should be applied to the cloud data as in Chosson et al. (2007). We will report results of these investigations in future publications.

**Acknowledgments.** This work was partially supported by the NOAA Grant NA05OAR4310107 (JS and WWG), by the 5.FP Project EVK2-CT2002-80010-CESSAR, KBN Grant SPUB-M, and PBS Grant ACCENT/295/2006 (JS and HP). Computer time was provided by NSF MRI Grants CNS-0421498, CNS-0420873, and CNS-0420985; NSF sponsorship of the National Center for Atmospheric Research and the University of Colorado; and a grant from the IBM Shared University Research (SUR) program. Comments on the manuscript by Hugh Morrison are acknowledged.

## REFERENCES

- Andrejczuk, M., W. W. Grabowski, S. P. Malinowski, and P. K. Smolarkiewicz, 2006: Numerical simulation of cloud–clear air interfacial mixing: Effects on cloud microphysics. *J. Atmos. Sci.*, **63**, 3204–3225.
- Baker, M. B., and J. Latham, 1979: The evolution of droplet spectra and the rate of production of embryonic raindrops in small cumulus clouds. *J. Atmos. Sci.*, **36**, 1612–1615.
- , R. G. Corbin, and J. Latham, 1980: The influence of entrainment on the evolution of cloud droplet spectra: I. A model of inhomogeneous mixing. *Quart. J. Roy. Meteor. Soc.*, **106**, 581–598.
- Blyth, A. M., 1993: Entrainment in cumulus clouds. *J. Appl. Meteor.*, **32**, 626–641.
- Brenguier, J.-L., and W. W. Grabowski, 1993: Cumulus entrainment and cloud droplet spectra: A numerical model within a two-dimensional dynamical framework. *J. Atmos. Sci.*, **50**, 120–136.
- Carpenter, R. L., Jr., K. K. Droegemeier, and A. M. Blyth, 1998: Entrainment and detrainment in numerically simulated cumulus congestus clouds. Part I: General results. *J. Atmos. Sci.*, **55**, 3417–3432.
- Chosson, F., J.-L. Brenguier, and M. Schröder, 2004: Radiative impact of mixing processes in boundary layer clouds. *Proc. 14th Int. Conf. on Clouds and Precipitation*, Bologna, Italy, International Association of Meteorology and Atmospheric Sciences, 371–374.
- , —, and L. Schüller, 2007: Entrainment-mixing and radiative transfer simulation in boundary layer clouds. *J. Atmos. Sci.*, **64**, 2670–2682.
- Grabowski, W. W., 2006: Indirect impact of atmospheric aerosols in idealized simulations of convective–radiative quasi equilibrium. *J. Climate*, **19**, 4664–4682.
- , and P. K. Smolarkiewicz, 1996: On two-time-level semi-Lagrangian modeling of precipitating clouds. *Mon. Wea. Rev.*, **124**, 487–497.
- Holland, J. Z., and E. M. Rasmusson, 1973: Measurements of the atmospheric mass, energy, and momentum budgets over a 500-kilometer square of tropical ocean. *Mon. Wea. Rev.*, **101**, 44–55.
- Kiehl, J. T., J. J. Hack, and B. P. Briegleb, 1994: The simulated earth radiation budget of the National Center for Atmospheric Research community climate model CCM2 and comparisons with the Earth Radiation Budget Experiment (ERBE). *J. Geophys. Res.*, **99**, 20 815–20 827.
- Margolin, L. G., P. K. Smolarkiewicz, and Z. Sorbjan, 1999: Large-eddy simulations of convective boundary layers using nonoscillatory differencing. *Physica D*, **133**, 390–397.
- Martin, G. M., D. W. Johnson, and A. Spice, 1994: The measurement and parameterization of effective radius of droplets in warm stratocumulus clouds. *J. Atmos. Sci.*, **51**, 1823–1842.
- McFarlane, S. A., and W. W. Grabowski, 2007: Optical properties of shallow tropical cumuli derived from ARM ground-based remote sensing. *Geophys. Res. Lett.*, **34**, L06808, doi:10.1029/2006GL028767.
- , K. F. Evans, and A. S. Ackerman, 2002: A Bayesian algorithm for the retrieval of liquid water cloud properties from microwave radiometer and millimeter radar data. *J. Geophys. Res.*, **107**, 4317, doi:10.1029/2001JD001011.
- Morrison, H., and W. W. Grabowski, 2007: Comparison of bulk and bin warm-rain microphysics models using a kinematic framework. *J. Atmos. Sci.*, **64**, 2839–2861.
- , and —, 2008: Modeling supersaturation and subgrid-scale mixing with two-moment bulk warm microphysics. *J. Atmos. Sci.*, **3**, 792–812.
- Pawlowska, H., and J.-L. Brenguier, 2000: Microphysical properties of stratocumulus clouds during ACE-2. *Tellus*, **52B**, 868–887.

- Siebesma, A. P., and Coauthors, 2003: A large eddy simulation intercomparison study of shallow cumulus convection. *J. Atmos. Sci.*, **60**, 1201–1219.
- Smolarkiewicz, P. K., and L. G. Margolin, 1997: On forward-in-time differencing for fluids: An Eulerian/semi-Lagrangian nonhydrostatic model for stratified flows. *Atmos.–Ocean*, **35**, 127–152.
- Stephens, G. L., 1978: Radiation profiles in extended water clouds. II: Parameterization schemes. *J. Atmos. Sci.*, **35**, 2123–2132.
- Stevens, B., and Coauthors, 2005: Evaluation of large-eddy simulations via observations of nocturnal marine stratocumulus. *Mon. Wea. Rev.*, **133**, 1443–1462.
- Stommel, H., 1947: Entrainment of air into a cumulus cloud. *J. Meteor.*, **4**, 91–94.
- Wang, Q., and B. A. Albrecht, 1994: Observations of cloud-top entrainment in marine stratocumulus clouds. *J. Atmos. Sci.*, **51**, 1530–1547.
- Warner, J., 1955: The water content of cumuliform cloud. *Tellus*, **7**, 449–457.